Eur. Phys. J. A **25**, 193–198 (2005)
DOI 10.1140/epja/i2005-10104-5

THE EUROPEAN PHYSICAL JOURNAL A

# Production cross-sections from neutron-deficient $^{92}$Mo at 500 A MeV

B. Fernández-Domínguez[1,a], R.C. Lemmon[2], B. Blank[3], M. Chartier[1], D. Cortina-Gil[4], J.L. Durell[5], H. Geissel[6], J. Gerl[6], S. Mandal[6], F. Rejmund[7], and K. Sümmerer[6]

[1] University of Liverpool, Oliver Lodge Laboratory, Physics Department, Oxford Street, Liverpool L69 7ZE, UK
[2] CLRC, Daresbury Laboratory, Daresbury, Warrington, WA4 4AD, UK
[3] CENBG, Le Haut Vigneau, F-33175 Gradignan Cedex, France
[4] Universidad de Santiago de Compostela, E-15706 Santiago de Compostela, Spain
[5] Schuster Laboratory, University of Manchester, Manchester M13 9PL, UK
[6] GSI, Planckstrasse 1, D-64291 Darmstadt, Germany
[7] GANIL, Bld. Henri Becquerel, B.P. 55027, F-14076 Caen Cedex 5, France

Received: 30 May 2005 / Revised version: 24 June 2005 /
Published online: 5 September 2005 – 
Communicated by J. Äystö

**Abstract.** The projectile fragmentation of a $^{92}$Mo beam onto a beryllium target at an incident energy of 500 $A$ MeV has been studied at the high-resolution spectrometer FRS at GSI. The isotopic production cross-sections of the projectile fragments produced in the reaction have been determined. The data have been compared to the empirical parameterisation, EPAX, and to a microscopic nuclear reaction model, ABRABLA.

**PACS.** 24.10.-i Nuclear reaction models and methods – 27.50.+e $59 \leq A \leq 89$

## 1 Introduction

There is great current interest in studying the structure of neutron-deficient nuclei with $N \simeq Z$ as it is expected that neutron-proton pairing correlations play an important role in the structure of such nuclei [1]. There is a near degeneracy of the proton and neutron Fermi surfaces and so protons and neutrons occupy identical orbitals. Thus, charge independence of the nuclear force implies that, for such nuclei, $T = 1$ $np$ pairing should exist on an equal footing with $T = 1$ $nn$ and $pp$ pairing. Strongly correlated $T = 0$ $np$ pairs should also exist in these nuclei.

However, the experimental evidence for $np$ pairing is scarce, largely because of the difficulty in producing such nuclei for study. Low-energy fusion-evaporation reactions with stable beams can be used to make $N \simeq Z$ nuclei but the production cross-sections are very low [2,3], the range of nuclei which are accessible is limited and the types of studies which can be performed restrictive. With the advent of new experimental facilities which can produce secondary beams of radioactive ions, $N \simeq Z$ nuclei can be produced more easily, making possible the use of the whole range of nuclear-structure techniques. As a consequence experimental and theoretical studies of $N \simeq Z$ nuclei are of great current interest. Fragmentation of intermediate and relativistic heavy-ion beams is widely used to produce secondary beams of exotic nuclei far from stability [4,5]. In order to assess the feasibility of experiments utilising secondary beams, a precise knowledge of the relevant production cross-sections is essential.

In this paper we report on the production cross-sections of nuclei produced via projectile fragmentation of a $^{92}$Mo beam at an incident energy of 500 $A$ MeV. Our interest in performing this experiment was to study the production cross-sections for the $N \simeq Z$ nuclei, which will extend the current database of production cross-sections of neutron-deficient fragments, reaching for some cases the proton dripline. The data can then be used to test the predictive power of the empirical parameterisations and fragmentation models. The database will be valuable in preparation for experiments to examine the structure of $N = Z$ nuclei.

## 2 Experimental procedure

The experiment was performed at the FRS facility at GSI in Darmstadt (Germany). The primary beam of $^{92}$Mo was delivered by the SIS synchrotron at an energy of 500 $A$ MeV. The average intensity was $10^9$ particles/spill.

[a] e-mail: bfd@ns.ph.liv.ac.uk

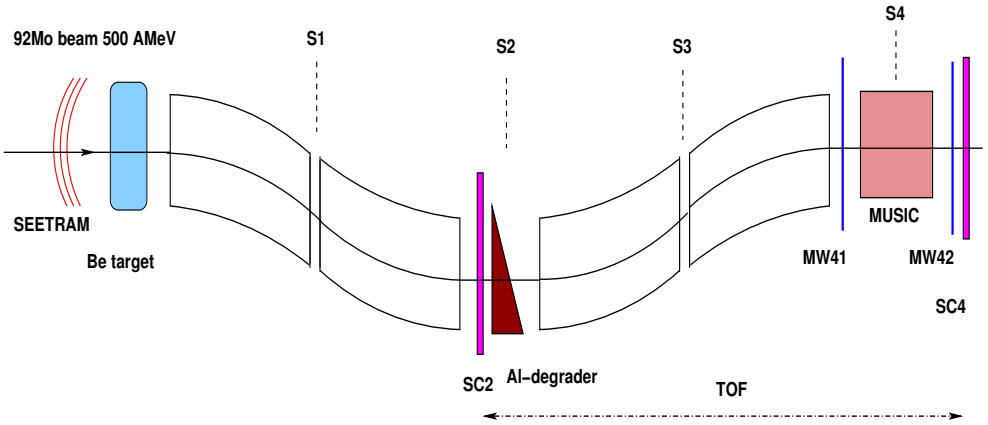


**Fig. 1.** Schematic diagram of the FRS set-up. The SEETRAM detector monitors the number of projectiles. The role of the plastic scintillators SC2 and SC4 is twofold: they are responsible for determining the TOF and the position measurements. The MUSIC provides the energy loss of the produced fragments and the multiwire chambers MW41, MW42 are used to determine the deviation from the central trajectory.

The $^{92}$Mo ions were directed onto a beryllium target of thickness 4007.0 mg/cm$^2$ placed at the entrance of the FRagment Separator, FRS [6]. The experimental set-up is displayed in fig. 1. The produced fragments were separated and analysed by means of the high-resolution magnetic spectrometer FRS. The number of incident ions was recorded by the secondary-electron monitor SEETRAM [7] placed before the production target. The projectile-like fragments passing through the spectrometer were identified in flight using a detector set-up consisting of two plastic scintillators (SC2, SC4) [8] mounted at the dispersive and achromatic focal planes, S2 and S4, respectively, one ionisation chamber (MUSIC) [9], and two multiwire chambers (MW41, MW42) [10]. A profiled aluminium degrader 816.75 mg/cm$^2$ thick was located at the intermediate focal plane S2 after the SC2 scintillator. The shape of the wedge was selected to ensure the achromatism of the ion-optical system [11].

The main goal of this experiment was the study of neutron-deficient fragments in the mass region $80 < A < 100$. Therefore, the FRS was optimised on different isotopes of the Zr element. In total, five settings were used: $^{86}$Zr, $^{84}$Zr, $^{82}$Zr, $^{80}$Zr and $^{78}$Zr. In addition, measurements optimised on the more neutron-rich nuclei $^{86}$Sr, $^{84}$Kr and $^{82}$Se, were also performed in order to cover the full isotopic distribution.

## 3 Isotopic identification of the ions

The ions of interest were identified by combining measurements of their magnetic rigidity ($B\rho$), energy loss ($\Delta E$), and time of flight (TOF). The plastic scintillators mounted at the dispersive intermediate and achromatic focal planes (S2, S4), were used to determine the horizontal positions of the fragments and their time of flight. At the final focal plane (S4) two multiwire chambers (MW41, MW42) provided the position measurement for the calibrations.

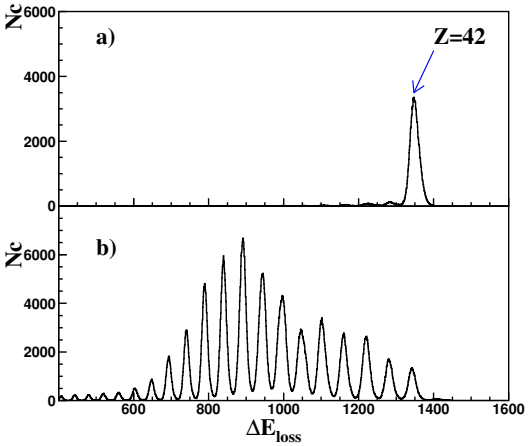


**Fig. 2.** a) Measured energy loss spectrum for the primary beam $^{92}$Mo. b) Response of the ionisation chamber, MUSIC, for the different fragments produced in several settings of magnetic rigidity of the spectrometer.

Finally, from the energy loss measurement in the ionisation chamber we obtained the nuclear charge ($Z$), since all the produced fragments were fully stripped ($q = Ze$) [12].

### 3.1 Charge identification

The charge identification was performed with the help of a setting centered on the primary beam, $Z = 42$. In fig. 2a) the energy loss spectrum of the primary beam is represented. Figure 2b) shows the energy loss spectrum of different elements measured in several settings. Therefore, the charge calibration was achieved by counting in $Z$ from the beam down to the lighter elements.

The charge resolution obtained was $\Delta Z = 0.42$ (FWHM). Therefore, the probability for misidentification in charge was lower than 6%.

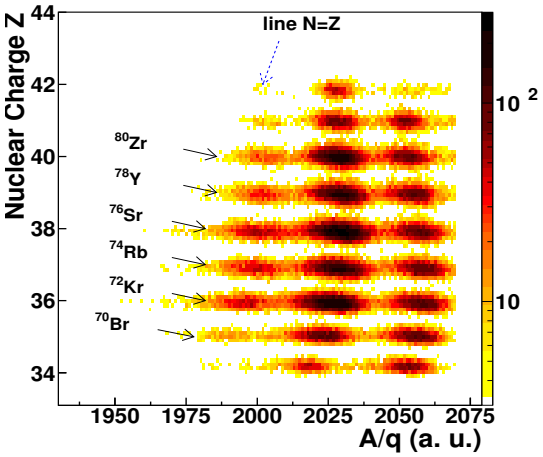


**Fig. 3.** Isotopic identification for a setting centered on $Z = 40$, $A = 80$.

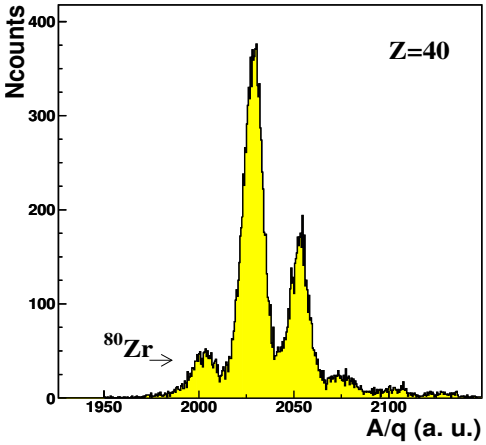


**Fig. 4.** Different $A/q$ values for the element $Z = 40$.

### 3.2 Mass calibration

From the magnetic rigidity ($B\rho$) and the time of flight (TOF) measurements we obtained the $A/q$ ratio for all the ions. A setting centered on the primary beam ($A/q = 2.19$) was used to calibrate the $A/q$ value of the fragments. Then the ions were identified by using the line $N = Z$ ($A/q = 2.0$) in the $Z$ *versus* the $A/q$ matrix. This procedure allowed us to assign a mass number to each fragment. Figure 3 shows the final ion identification plot for a setting optimised on $^{80}$Zr.

Figure 4 shows the projection onto the $A/q$ axis for a given charge $Z = 40$. The probability for misidentification was below 2% for the data centered on the isotopes of the element $Z = 40$ (neutron-deficient settings).

In the settings centered on the more neutron-rich nuclei, due to a continuous background in the TOF measurement, this probability was as large as 33% for those nuclei in the settings close to the stability line.

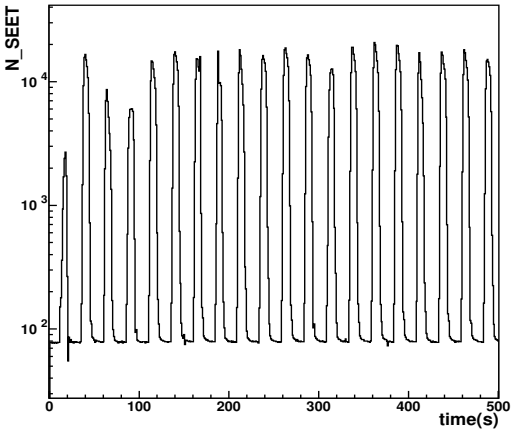


**Fig. 5.** Spill structure of the beam recorded in the SEETRAM detector as a function of time (in seconds) for a setting centered on $^{84}$Kr.

## 4 Experimental production cross-sections

The production cross-section for each nuclide was extracted using the following expression:

$$\sigma(Z,A) = \frac{Y(Z,A)}{N_{\rm pro} \cdot N_{\rm at} \cdot \epsilon \cdot \tau \cdot f_{\rm trans}}\,, \qquad (1)$$

where $Y(Z,A)$ is the number of counts detected for each fragment of nuclear charge $Z$ and mass number $A$. The $N_{\rm pro}$ factor is the number of incident projectiles and $N_{\rm at}$ is the number of atoms in the target, which is 0.287 at/barn. The factors $\epsilon$ and $\tau$ correct for the efficiency of the detectors and the lifetime of the data acquisition, respectively. Finally, $f_{\rm trans}$ accounts for the transmission of the fragments through the spectrometer. This factor also includes losses due to secondary reactions in the target as well as in the different material layers along the beam line. The total identification efficiency of the detectors including the lifetime of the data acquisition varied from 36% to 84%. The rest of the factors are discussed in the next sections.

### 4.1 Separator transmission

The estimation of the transmission of fragments through the FRS spectrometer was obtained using the simulation programs, Lieschen [13] and LISE++ [14], setting by setting. The resulting factor $f_{\rm trans}$ used in eq. (1) is the average value of the calculations given by both programs. The transmission drops drastically from 38% for the central fragments to 1% for the ions at the limits of the acceptance of the spectrometer. In the present analysis, we have only considered ions with a transmission higher than 1%. Some nuclei were measured in different settings and reasonable agreement of the cross-sections between the overlapping isotopes was found.

The uncertainty associated with the transmission value was obtained from the differences in the transmission

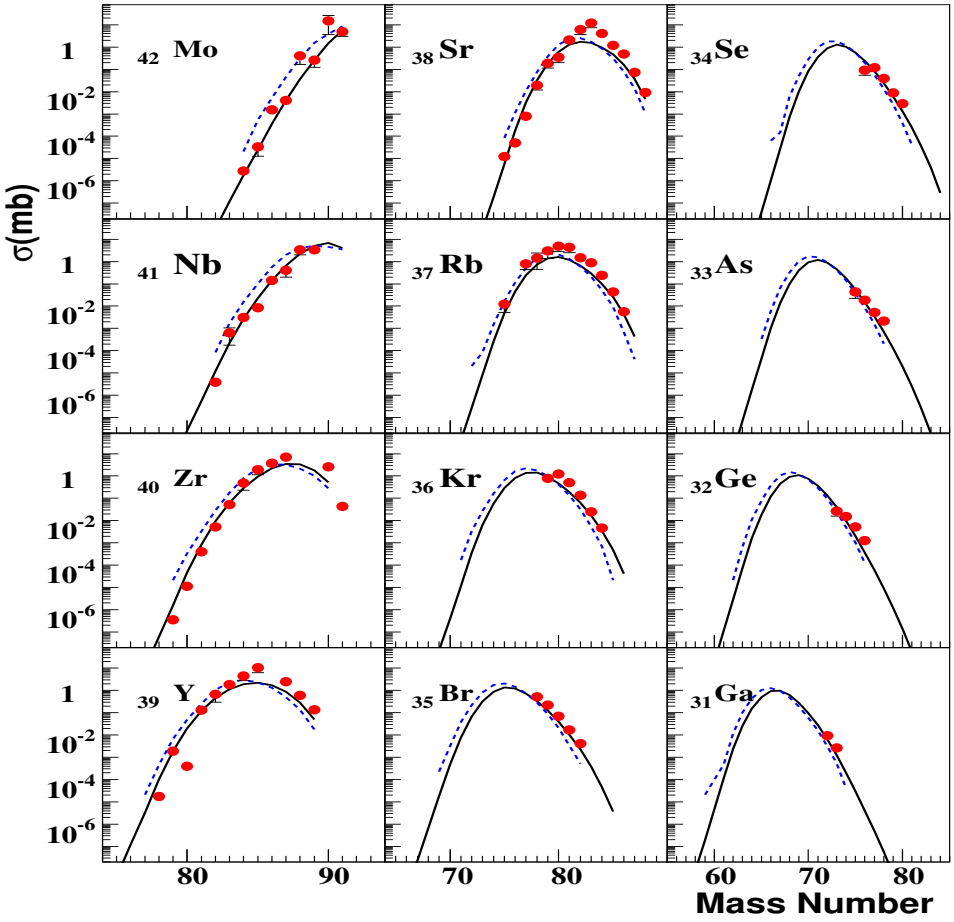


**Fig. 6.** Isotopic production cross-sections in mb. The total uncertainty is shown when exceeding the size of the points. The solid lines correspond to the values obtained from EPAX [15], and the dashed lines to the predictions from ABRABLA [16].

calculated with both codes. Furthermore, ions with a difference higher than 75% between both calculations were rejected. Although the threshold value is somehow arbitrary it was chosen in order to keep the transmission uncertainty lower than 100%

### 4.2 Primary-beam intensity

During the experiment the spill structure of the beam was monitored by the secondary electron detector SEETRAM (see fig. 1). However, this detector does not provide a direct measurement of the number of projectiles. Therefore, a calibration is needed in order to estimate the number of incident particles associated with each count in SEETRAM. Hence, the number of projectiles $N_{\mathrm{pro}}$ of eq. (1) can be expressed as: $N_{\mathrm{pro}} = N_{\mathrm{SEET}} \cdot f_{\mathrm{SEET}} \cdot S$, where $N_{\mathrm{SEET}}$ is the number of SEETRAM counts detected related to the beam intensities, $f_{\mathrm{SEET}}$ is the calibration factor and $S$ is the sensitivity of SEETRAM detector. The calibration of the SEETRAM was carried out with a scintillator, by increasing gradually the beam intensity. The relation between the number of counts in the scintillator and the number of counts in the SEETRAM led to a calibration factor $f_{\mathrm{SEET}} = 698.69 \pm 8.99$ for a sensitivity of $10^{-10}$.

**Table 1.** Mean systematical uncertainties contributing to the determination of the production cross-sections expressed in %.

| | Uncertainty (%) |
|---|---|
| Target thickness | $\Delta(N_{\mathrm{at}}) = 0.1$ |
| SEETRAM calibration | $\Delta(F_{\mathrm{SEET}}) = 1$ |
| SEETRAM offset | $\Delta(F_{\mathrm{off}}) = 2$–$54$ |
| Transmission | $\Delta(f_{\mathrm{trans}}) = 10$–$75$ |
| Statistical | $\Delta(\mathrm{stat}) = 1$–$33$ |
| Total mean uncertainty | $\Delta_{\mathrm{tot}} = 10$–$90$ |

Figure 5 shows the spectrum of the total number of counts in the SEETRAM ($N_{\mathrm{SEET}}$) as a function of time in seconds for a setting centered on $Z = 36$ and $A = 84$. The counts between two spills are related to the dark current in the detector. This contribution can be removed by subtracting an offset. Finally, from the integration of the spectrum after subtracting the dark current, we obtain $N_{\mathrm{SEET}}$.

The uncertainty associated with the number of counts in SEETRAM is related to the uncertainty in the

**Table 2.** Measured cross-sections in mb for the different fragments produced in the reaction $^{92}$Mo + $^{9}$Be at 500 $A$ MeV.

| $Z$ | $A$ | $\sigma$ (mb) | $Z$ | $A$ | $\sigma$ (mb) | $Z$ | $A$ | $\sigma$ (mb) |
|---|---|---|---|---|---|---|---|---|
| 31 | 72 | $0.94(30)\,E-2$ | 37 | 80 | $0.49(21)\,E+1$ | 39 | 88 | $0.59(2)\,E+0$ |
| 31 | 73 | $0.27(5)\,E-2$ | 37 | 81 | $0.44(18)\,E+1$ | 39 | 89 | $0.14(1)\,E+0$ |
| 32 | 73 | $0.27(11)\,E-1$ | 37 | 82 | $0.15(1)\,E+1$ | 40 | 79 | $0.04(0)\,E+0$ |
| 32 | 74 | $0.15(3)\,E-1$ | 37 | 83 | $0.87(5)\,E+0$ | 40 | 80 | $0.11(0)\,E-4$ |
| 32 | 75 | $0.51(8)\,E-2$ | 37 | 84 | $0.24(2)\,E+0$ | 40 | 81 | $0.39(9)\,E-3$ |
| 32 | 76 | $0.12(3)\,E-2$ | 37 | 85 | $0.44(4)\,E-1$ | 40 | 82 | $0.52(8)\,E-2$ |
| 33 | 75 | $0.43(21)\,E-1$ | 37 | 86 | $0.57(13)\,E-2$ | 40 | 83 | $0.52(15)\,E-1$ |
| 33 | 76 | $0.18(4)\,E-1$ | 38 | 75 | $0.12(4)\,E-4$ | 40 | 84 | $0.48(25)\,E+0$ |
| 33 | 77 | $0.53(8)\,E-2$ | 38 | 76 | $0.51(19)\,E-4$ | 40 | 85 | $0.19(8)\,E+1$ |
| 33 | 78 | $0.22(4)\,E-2$ | 38 | 77 | $0.78(19)\,E-3$ | 40 | 86 | $0.38(13)\,E+1$ |
| 34 | 76 | $0.92(38)\,E-1$ | 38 | 78 | $0.20(8)\,E-1$ | 40 | 87 | $0.69(26)\,E+1$ |
| 34 | 77 | $0.12(1)\,E+0$ | 38 | 79 | $0.19(8)\,E+0$ | 40 | 90 | $0.25(2)\,E+1$ |
| 34 | 78 | $0.39(5)\,E-1$ | 38 | 80 | $0.35(15)\,E+0$ | 40 | 91 | $0.44(10)\,E-1$ |
| 34 | 79 | $0.89(16)\,E-2$ | 38 | 81 | $0.21(7)\,E+1$ | 41 | 82 | $0.39(5)\,E-5$ |
| 34 | 80 | $0.29(4)\,E-2$ | 38 | 82 | $0.61(25)\,E+1$ | 41 | 83 | $0.62(44)\,E-3$ |
| 35 | 78 | $0.52(13)\,E+0$ | 38 | 83 | $0.12(5)\,E+2$ | 41 | 84 | $0.31(6)\,E-2$ |
| 35 | 79 | $0.22(3)\,E+0$ | 38 | 84 | $0.40(10)\,E+1$ | 41 | 85 | $0.86(23)\,E-2$ |
| 35 | 80 | $0.70(8)\,E-1$ | 38 | 85 | $0.12(0)\,E+1$ | 41 | 86 | $0.14(5)\,E+0$ |
| 35 | 81 | $0.17(2)\,E-1$ | 38 | 86 | $0.49(4)\,E+0$ | 41 | 87 | $0.40(20)\,E+0$ |
| 35 | 82 | $0.42(5)\,E-2$ | 38 | 87 | $0.72(4)\,E-1$ | 41 | 88 | $0.33(13)\,E+1$ |
| 36 | 79 | $0.77(6)\,E+0$ | 38 | 88 | $0.92(20)\,E-2$ | 41 | 89 | $0.33(11)\,E+1$ |
| 36 | 80 | $0.12(1)\,E+1$ | 39 | 78 | $0.17(1)\,E-4$ | 42 | 84 | $0.28(5)\,E-5$ |
| 36 | 81 | $0.51(4)\,E+0$ | 39 | 79 | $0.19(6)\,E-2$ | 42 | 85 | $0.33(20)\,E-4$ |
| 36 | 82 | $0.14(1)\,E+0$ | 39 | 80 | $0.40(8)\,E-3$ | 42 | 86 | $0.15(4)\,E-2$ |
| 36 | 83 | $0.24(3)\,E-1$ | 39 | 81 | $0.13(4)\,E+0$ | 42 | 87 | $0.40(10)\,E-2$ |
| 36 | 84 | $0.47(9)\,E-2$ | 39 | 82 | $0.68(39)\,E+0$ | 42 | 88 | $0.41(24)\,E+0$ |
| 37 | 75 | $0.12(7)\,E-1$ | 39 | 83 | $0.18(6)\,E+1$ | 42 | 89 | $0.26(13)\,E+0$ |
| 37 | 77 | $0.78(35)\,E+0$ | 39 | 84 | $0.45(17)\,E+1$ | 42 | 90 | $0.15(11)\,E+2$ |
| 37 | 78 | $0.14(10)\,E+1$ | 39 | 85 | $0.10(4)\,E+2$ | 42 | 91 | $0.49(19)\,E+1$ |
| 37 | 79 | $0.30(16)\,E+1$ | 39 | 87 | $0.25(1)\,E+1$ | | | |

determination of the offset. In the case of the runs optimized on $^{86}$Sr, $^{84}$Kr, $^{82}$Se and $^{82}$Zr, the offset was so well defined (error below $\Delta(F_{\rm off}) = 0.02\%$) that the uncertainty in the number of counts in the SEETRAM can be neglected.

However, for the runs centered on $^{86}$Zr, $^{84}$Zr, $^{80}$Zr and $^{78}$Zr, the dark current fluctuated considerably. In order to take this effect into account, an average offset was determined, the error in the number of SEETRAM counts was derived from the standard deviation. In some cases, the final uncertainty reached up to $\Delta(F_{\rm off}) = 54\%$ for the most exotic settings.

### 4.3 Overall uncertainties

The total uncertainty on the cross-section is essentially dominated by the transmission uncertainty.

The statistical uncertainty was calculated as

$$\Delta(\mathrm{stat}) = \Delta(Nc)^2 + \Delta(Sep)^2\,, \qquad (2)$$

where $\Delta(Nc)$ is the uncertainty in the number of counts inside each contour, and $\Delta(Sep)$ corresponds to the probability of misidentification. The total statistical uncertainty remains lower than 5% for most of the nuclides. However, for the most exotic cases it can reach 30%.

Table 1 lists the typical values of the uncertainties attributed to each factor in eq. (1).

### 4.4 Results

The isotopic production cross-sections of 12 elements measured in this experiment from $Z = 31$ up to $Z = 42$ are shown in fig. 6 (see table 2 for quantitative results).

As mentioned above, we present experimental cross-sections only for isotopes which have a transmission of at least 1% and for which the two simulations used to determine the trasnmission agree to better than 75%.

## 5 Discussion

In this section we will compare our experimental data to the predictions of the semi-empirical parameterisation EPAX [15], and to the nuclear reaction model ABRABLA [16].

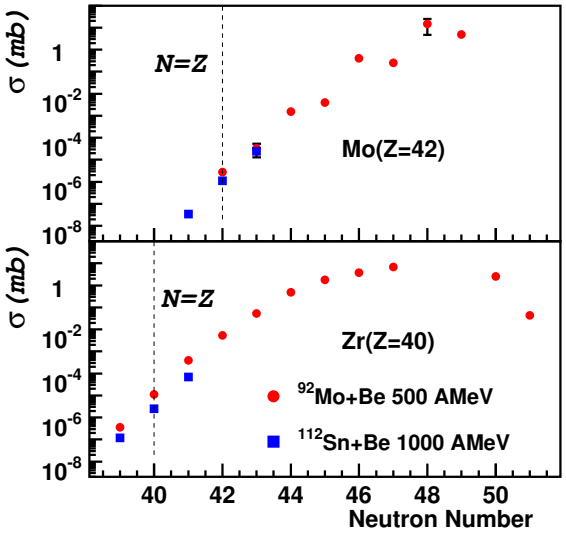


**Fig. 7.** Cross-section in mb *versus* the neutron number for the elements Mo ($Z = 42$) and Zr ($Z = 40$), respectively. The experimental data obtained in this work are represented by the circles and the results measured by Stolz *et al.* [4] by the squares.

### 5.1 Comparison with model predictions.

In fig. 6, the experimental data are compared to the predictions from the EPAX parameterisation (solid lines), [15], and to the values obtained from the geometrical abrasion-ablation model ABRABLA (dashed lines), [16,17].

On the neutron-rich side of the distributions of the elements $31 < Z < 40$, EPAX and ABRABLA are in agreement with the experimental data. However, on the neutron-deficient side, EPAX gives better agreement, whereas ABRABLA tends to overestimate the cross-sections. This may be due to an overestimation of the excitation energy of the prefragment at the end of the first step of the reaction.

It can be noticed that the ridge of the experimental isotopic distribution for the elements $37 \leq Z \leq 39$ shows a sharp peak. The isotopes in this region were mainly measured in the setting centered on $^{86}$Zr and for this measurement the lifetime of the acquisition was only around 35%. Thus, it is likely that the rise might come from some fluctuations in the spill structure.

### 5.2 Comparison with experimental data from the literature

Our data have been compared to the results obtained by Stolz *et al.* [4] from the fragmentation of $^{112}$Sn at 1000 $A$ MeV. In fig. 7 the comparison is presented for two elements Zr ($Z = 40$) and Mo ($Z = 42$). It can be seen that the production of the nuclei with $N = Z = 30$–40 is higher when using the reaction $^{92}$Mo + $^{9}$Be.

This can be easily understood, since the production is higher closer to the projectile and it decreases when the number of nucleons removed from the projectile increases. Since the isotopes of the Zr ($Z = 40$) and Mo ($Z = 42$) elements produced in the fragmentation of $^{112}$Sn are far away from the projectile (8–10 charges below), this behaviour confirms that the $^{92}$Mo beam is a better choice for planning future experiments to study nuclei near the $N \simeq Z$ line in the mass region $80 < A < 90$.

## 6 Conclusions

The nuclei produced in the fragmentation of $^{92}$Mo at 500 $A$ MeV have been identified in charge and mass number. The isotopic production cross-sections for twelve elements ranging from $Z = 31$ (Ga) up to $Z = 42$ (Mo) have been measured. The experimental results have been compared to the empirical parameterisation EPAX, and to a microscopic nuclear reaction model, ABRABLA. An overall better agreement of the data with EPAX has been observed. The comparison with ABRABLA shows an overestimation of the production on the neutron-deficient side of the isotopic distribution. In addition, the production cross-sections were compared to the experimental results measured in a previous work where the fragmentation of $^{112}$Sn at 1000 $A$ MeV has been studied. From this comparison, the projectile fragmentation of $^{92}$Mo is shown to be a better choice to produce the neutron-deficient fragments in the $N = Z = 30$–40 region.

We would like to thank the FRS staff for their assistance with the tuning of the experimental set-up during the measurements. This work was supported in part by the Royal Society and the United Kingdom Engineering and Physical Sciences Research Council.

## References

1. D. Rudolph, M. Hellstrom (Editors), *Selected Topics on $N = Z$ Nuclei* (Bloms i Lund AB, Lund, Sweden, 2000).
2. D. Rudolph *et al.*, Phys. Rev. C **69**, 034309 (2004).
3. D.G. Jenkins *et al.*, Phys. Rev. C **65**, 064307 (2002).
4. A. Stolz *et al.*, Phys. Rev. C **65**, 064603 (2002).
5. S.J. Yennello *et al.*, Phys. Rev. C **46**, 2620 (1992).
6. H. Geissel *et al.*, Nucl. Instrum. Methods B **70**, 286 (1992).
7. C. Ziegler *et al.*, GSI Scientific Report 1990, No. GSI 91-1 (1991) p. 291.
8. B. Voss *et al.*, Nucl. Instrum. Methods A **364**, 150 (1995).
9. M. Pfützner *et al.*, Nucl. Instrum. Methods B **86**, 213 (1994).
10. H. Stelzer *et al.*, Nucl. Instrum. Methods A **310**, 103 (1991).
11. K.-H. Schmidt *et al.*, Nucl. Instrum. Methods A **260**, 260 (1987).
12. C. Scheidenberger *et al.*, Nucl. Instrum. Methods B **141**, 441 (1998).
13. `http://www-w2k.gsi.de/kschmidt/software.htm`.
14. D. Bazin *et al.*, Nucl. Instrum. Methods A **482**, 307 (2002).
15. K. Sümmerer, B. Blank, Phys. Rev. C **61**, 034607 (2000).
16. J.J. Gaimard, K.H. Schmidt, Nucl. Phys. A **531**, 709 (1991).
17. A.R. Junghans *et al.*, Nucl. Phys. A **629**, 635 (1998).